Analysis of admittance control for a fully-actuated, tactile UAV

Iris Liu*, Suvarna Swaraj, Karl Stol and Salim Al-zubaidi
Department of Mechanical and Mechatronics Engineering, University of Auckland, New Zealand

ABSTRACT

Abstract— The main contribution of this paper is the tuning of an admittance controller on a compact, fully-actuated, multirotor Unmanned Aerial Vehicle (UAV) for the purpose of achieving optimal, intuitive, physical human drone interaction (PHDI). The controller permits a human to physically translate and rotate the UAV in flight while minimizing reaction forces and moments. Being a fully-actuated UAV allows the translation and rotation to be decoupled. The performance of the admittance controller was validated through simulations and experimental testing; optimal reaction forces of 0.7% and 1.3% of the UAV's weight were achieved for translation in the horizontal axis in simulations and free flight tests, respectively.

1 INTRODUCTION

The prevalence of physical human drone interaction (PHDI) has been rising in recent years due to their importance in various applications such as search and rescue [1], augmented drone ball sports [2], assisting the visually impaired [3], and enhancing the virtual reality (VR) gaming experience through haptic feedback [4]. Literature focused on physical or touch based interaction with UAVs improves knowledge of different techniques used to estimate the external forces and torques applied to the UAV during an interaction, and controllers which regulate the UAV's resultant behavior.

The performance of PHDI can be influenced by the UAV rotor configuration. Underactuated UAVs are categorized as having less actuators than the number of degrees of freedom (DoF). They are widely accessible and simply constructed, however, have coupled rotational and translational dynamics. The intrinsic underactuation of such conventional quadrotors may inhibit the PHDI performance and cause safety concerns [5]. Existing studies have explored PHDI with underactuated UAVs such as use of small quadcopters that act as haptic-input devices for greater immersion of the user in a VR game [4]. Similarly, Braley et al. [6] investigated stackable nanocopters which can be physically deformed by the user for the purpose of representing voxel grids for 3D spatial transformations. Underactuated UAVs are suitable for PHDI when they are required to be small, compact, inexpensive, and for a swarm. However, interactions that lack intuition can result due to their coupled translational and rotational dynamics, such as for a safe-to-touch quadcopter built by Abtahi et al. [7].

*Email address: sliu142@aucklanduni.ac.nz

Figure 1: User physically interacting with a multirotor UAV

An opportunity exists to exploit the capabilities of fully-actuated UAVs for PHDI, where the translational and rotational dynamics are decoupled. Improved omni-directional motion and agility are key advantages of fully-actuated UAVs over their underactuated counterparts [8]. In a wider context, research into physical drone interactions have been conducted on a fully-actuated drone [9], and the ability to independently control the linear and angular accelerations allowed for precise interactions with static objects to be made.

Admittance control has been widely used in human robot interaction applications for generating compliant trajectories such as stabilized stair climbing for humanoid robots [10] and control of a robotic exoskeleton [11]. Augugliaro et al. [12] demonstrated the ability of an admittance controller to adjust a quadcopter's reference trajectory to comply with an interaction. This indicates the merit of extending research into using admittance control to regulate the behavior of a fully-actuated UAV during interaction. An admittance controller seeks to make the closed loop behavior of the UAV match a mass-spring-damper system using the estimated external wrench during the interaction. The admittance controller parameters, mass, spring, and damping, can be tuned intuitively based upon the behavior desired from the UAV, as shown in [13]. Rajappa et al. [5] simulated use of admittance control to regulate the behavior of a fully-actuated hexarotor. To the best of the authors' knowledge, this is the only study in literature currently that explores the use of admittance control for a fully-actuated UAV in the area of PHDI. The work in this paper differs as the concept was experimentally tested and optimized. The hexarotor in [5] was able to translate to a new position with minimal changes to its attitude; hence showcasing the dexterity of a fully-actuated UAV in PHDI. A force sensor ring was installed on the UAV to perform external wrench estimation. Due to the potential loss in flight time, added weight, and power consumed, additional hardware is not a practical option for interaction wrench detection in this research. Software based methods of interaction detection to estimate the external wrench could, therefore, be more appropriate. These include an approach proposed by Tomic et al. [14] where a hybrid momentum-acceleration-based estimator was used by exploiting onboard sensors.

The work conducted in this paper involves the tuning of an admittance controller for regulating the behavior of a fully-actuated, stacked, fixed-tilt, octorotor during physical interaction. The performance of the controller is validated in simulation and experiments for multiple translational and rotational axes. Additionally, simulations and optimization in the roll-axis showcase the unique capability of a fully-actuated UAV to station keep at a non-zero roll angle after interaction, allowing its use in a greater range of applications.

2 Multirotor UAV Model

The fully-actuated multirotor used in this study is based on the octorotor in [15], featuring a compact, stacked rotor design (Figure 2). It has a flying mass of 985g and hover time of 14 minutes. To achieve safe and effective PHDI, an interaction frame and propeller guards were designed and attached onto the UAV, pictured in Figure 3. The added frame results in an additional 280g in the UAV's mass; a total flight mass of 1265g. The safety and mechanical design requirements of the interaction frame achieved are: a minimum clearance of 20 mm between the added features and the rotor blades, and a minimum clearance of 200 mm between the handle and the rotor blades. The position vector is defined as $\boldsymbol{\xi} = [x, y, z]$ and the rotational vector is expressed using the Euler angle conventions of $\boldsymbol{\eta} = [\phi, \theta, \psi]$, corresponding to roll, pitch, and yaw, respectively.

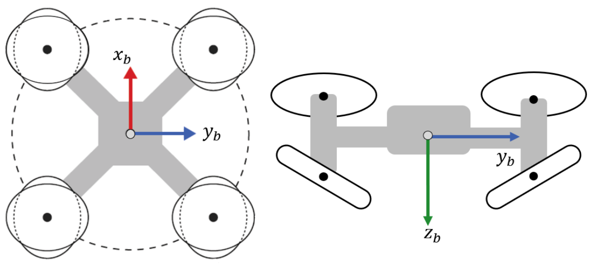

Figure 2: Schematic of stacked multirotor and configuration of tilted rotors about the orthogonal axes

For the purpose of the work conducted in this paper, all external forces measured are assumed to be from the human interaction and disturbances, such as wind, are negligible.

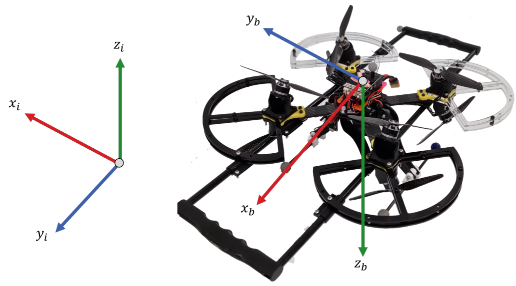

Figure 3: PHDI setup with a fully-actuated stacked multirotor and the designed interaction frame based on the concept from [15]. Subscripts b and i denote body and inertial frames, respectively.

3 Control System Architecture

The control system architecture design, as shown in Figure 4, consists of five main components:

1. The standard cascaded P-PID controllers of the PX4 firmware, namely position and attitude controllers, which provide position/velocity and angle/angular rate control, respectively.
2. The motor mixer which produces the motor setpoints in the form of PWM signals.
3. Human external wrench from the physical interaction ($\boldsymbol{f_{ext}}$ and $\boldsymbol{\tau_{ext}}$).
4. An external wrench estimator, based on the one used by Tomić et al. [14], which takes in the measured acceleration ($\ddot{\boldsymbol{\xi}}_{\boldsymbol{meas}}$) and angular velocity ($\dot{\boldsymbol{\eta}}_{\boldsymbol{meas}}$) to estimate the forces and moments, $\boldsymbol{f_e}$ and $\boldsymbol{\tau_e}$, respectively, applied by the human during the interaction. The estimator utilizes a hybrid momentum-acceleration-based approach, together with the onboard inertial measurement unit (IMU) and the UAV's dynamics model to provide wrench estimation.
5. The admittance controller, which takes in the estimated wrench and calculates new position and attitude setpoints, $\boldsymbol{\xi_{SP,AC}}$ and $\boldsymbol{\eta_{SP,AC}}$, which provide references for the subsequent controllers.

3.1 Admittance Controller

Admittance controllers are commonly used in human-robot interactions to achieve compliant trajectories based on the applied interaction forces and moments. A second order mass-spring-damper system is used to describe the desired characteristics of the closed-loop position and attitude control systems.

Equation 1 represents the desired closed-loop system dynamics:

$$\boldsymbol{M}\begin{bmatrix}\ddot{\boldsymbol{\xi}}\\ \ddot{\boldsymbol{\eta}}\end{bmatrix} + \boldsymbol{C}\begin{bmatrix}\dot{\boldsymbol{\xi}}\\ \dot{\boldsymbol{\eta}}\end{bmatrix} + \boldsymbol{K}\begin{bmatrix}\boldsymbol{\xi}\\ \boldsymbol{\eta}\end{bmatrix} = \begin{bmatrix}\boldsymbol{f_e}\\ \boldsymbol{\tau_e}\end{bmatrix} \tag{1}$$

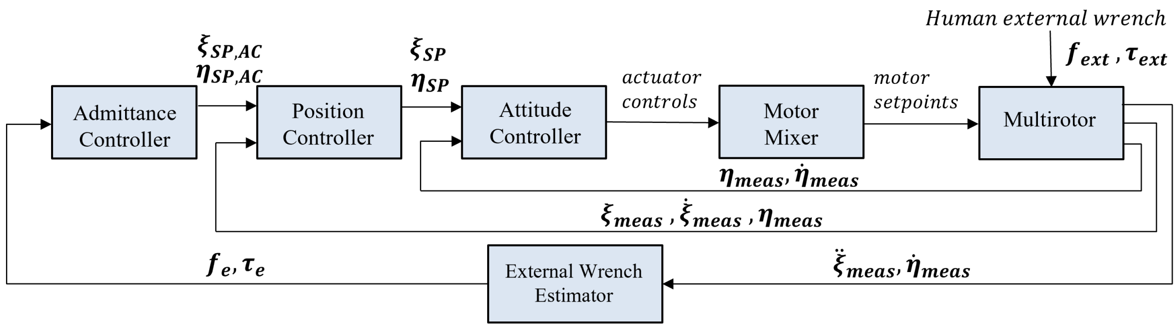

Figure 4: Control system architecture

where
$M = diag\{m_x \quad m_y \quad m_z \quad m_\phi \quad m_\theta \quad m_\psi\}$,
$C = diag\{c_x \quad c_y \quad c_z \quad c_\phi \quad c_\theta \quad c_\psi\}$,
$K = diag\{k_x \quad k_y \quad k_z \quad k_\phi \quad k_\theta \quad k_\psi\}$,
$f_e = diag\{f_{e,x} \quad f_{e,y} \quad f_{e,z} \quad f_{e,\phi} \quad f_{e,\theta} \quad f_{e,\psi}\}$,
$\tau_e = diag\{\tau_{e,x} \quad \tau_{e,y} \quad \tau_{e,z} \quad \tau_{e,\phi} \quad \tau_{e,\theta} \quad \tau_{e,\psi}\}$.
M, C, K, f_e, τ_e correspond to the mass, damping, spring, and estimated force and moment matrices, respectively. Note that the parameters in the y and pitch axes have been set as equal to the corresponding x and roll axes, respectively, as similar behavior is expected. As the objective is to reduce the experienced reaction wrench from the UAV, K has been set to the zero matrix to enable passive accommodation control; this has been seen in similar studies involving admittance control for human UAV interactions [16].

The output of the admittance controller is a vector of setpoints, therefore the control laws for the position and attitude are Equations 2 and 3, respectively.

$$\xi_{SP,AC}(s) = \frac{f_e(s)}{Ms^2 + Cs} \tag{2}$$

$$\eta_{SP,AC}(s) = \frac{\tau_e(s)}{Ms^2 + Cs} \tag{3}$$

4 SIMULATION

4.1 Simulation Model

From Figure 4, the simulated multirotor models the frame and each rotor as independent rigid bodies. Aerodynamic forces are limited to quasi-steady thrusts and torques acting at each rotor; aerodynamic forces due to UAV motion through still air are ignored. The human external wrench is modeled using a human external wrench emulator. For the force emulator, this takes an input of the UAV's final position, ξ_f , and duration of interaction, t_d, as specified by the user. The reference acceleration profile, $\ddot{\xi}_{ref}$, is computed as shown in Equation 4. As shown in Equation 5, a PID controller, $C(s)$, acts on $E_\xi(s)$, the difference between the reference, ξ_{ref} , and the actual position, ξ_{meas}, and outputs the simulated external forces, f_{ext}, to be applied to the multirotor plant. The moment emulator follows the same method to simulate external moments, τ_{ext}.

$$\ddot{\xi}_{ref}(s) = \frac{4\xi_f}{t_d^2} \tag{4}$$

$$f_{ext} = C(s)E_\xi(s) \tag{5}$$

In order to achieve PHDI, the external wrench must be estimated accurately. The estimated forces and moments are compared against the output of the human emulator. Figures 5(a) and (b) illustrate the wrench estimator and human emulator comparison for the x and roll axes, respectively. In both cases, the estimated forces and moments appear to follow the emulated profiles, thus, the estimator appears to accurately estimate the forces and moments. A deviation is observed in the second half of moment estimation in Figure 5(b). This could be attributed to tuning of gains required for the magnitude of the moments to match.

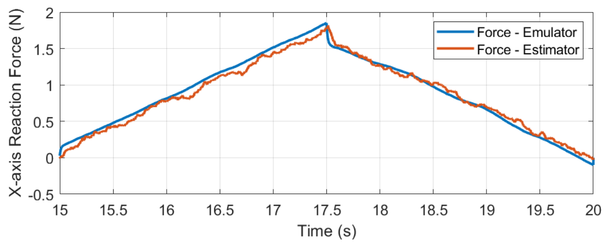

(a)

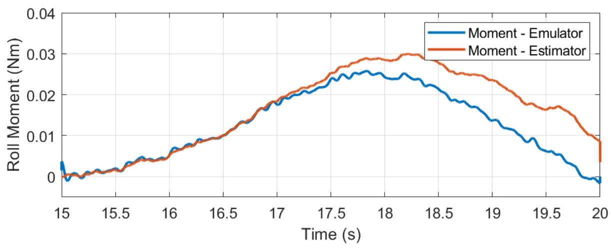

(b)

Figure 5: External wrench estimation performance for (a) x-axis and (b) roll-axis

(a) (b)

Figure 6: Parameter sweep of m_x and c_x values for (a) a 1m x-axis drag and m_ϕ and c_ϕ for (b) a 5deg roll-axis drag simulations to optimize for minimal RMS reaction force and moment, respectively, during interaction. Red circle indicates the optimal point for each of the parameter sweeps.

(a) (b)

Figure 7: Relationship between changing c_x with RMS reaction force for (a) a 1m x-axis drag and c_ϕ with RMS reaction moment for (b) a 5deg roll-axis drag simulation at optimal m_x and m_ϕ of zero

4.2 Test Procedure

The work in this paper focuses on a drag interaction which involves specifying a final displacement, $\boldsymbol{\xi_f}$ and $\boldsymbol{\eta_f}$, for the UAV to reach at the end of the interaction, and begins and ends at rest. The duration of the interaction was set to $t_d = 5s$ and began at time, $t = 15s$. Note that for the purpose of understanding, positive z has been defined as upwards, as defined in the inertial coordinate system.

Drag interactions were simulated for five single-DoF cases:

1. x-translational drag - $\boldsymbol{\xi_f} = (1, 0, 0)m$
2. z-translational drag up - $\boldsymbol{\xi_f} = (0, 0, 1)m$
3. z-translational drag down - $\boldsymbol{\xi_f} = (0, 0, -1)m$
4. Yaw-axis drag - $\boldsymbol{\eta_f} = (0, 0, 45)deg$
5. Roll-axis drag - $\boldsymbol{\eta_f} = (5, 0, 0)deg$

The duration of interaction for analysis of data is defined as when the admittance controller first updates new setpoints until it stops. To achieve a high level of compliance, the aim is to obtain as low a reaction force or moment as possible, thus the objective function is to minimize the estimated force or moment during interaction. The scope of the paper focuses on the interaction stage, over which the root mean square (RMS) force and moment are calculated.

4.3 Results and Discussion

From Figure 6, three main trends are observed in both cases:

1. For a constant mass, the RMS reaction force and moment increases with increasing damping. This aligns well with Equation 1, where the damping force is proportional to the damping coefficient for a set velocity. As the velocity in the concerned axis is fairly consistent across the tested cases, a high reaction force and moment is expected as damping increases.

2. For constant damping, the RMS reaction force and moment increases with increasing mass. A heavier mass suggests a larger force and moment is required to accelerate the system, hence resulting in this observed trend.

3. Turning points are observed at low damping values where the RMS reaction force and moment increases significantly. A finer c_i step size of $0.01Ns/m$ was then used to capture the trends near the optimal point. Figures 7(a) and (b) illustrate the local minima by sweeping through damping coefficients. A clear turning point is observed for both cases and the damp-

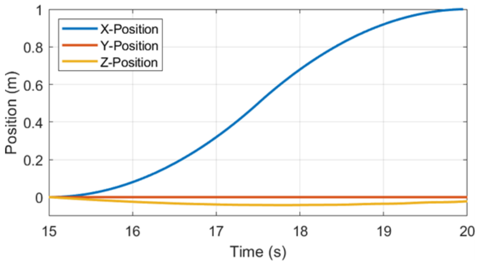

(a)

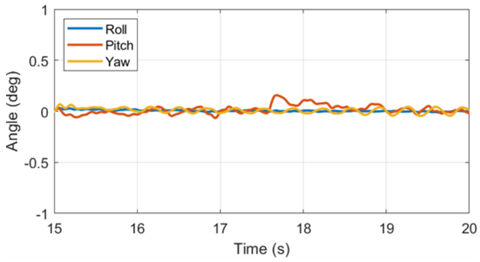

(b)

Figure 8: (a) Position and (b) attitude plots for the 1m x-axis drag

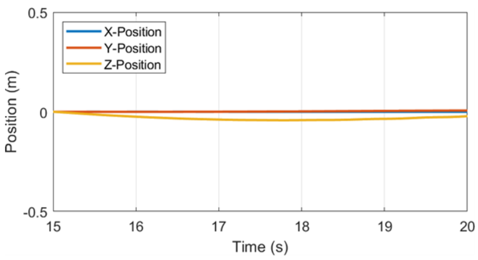

(a)

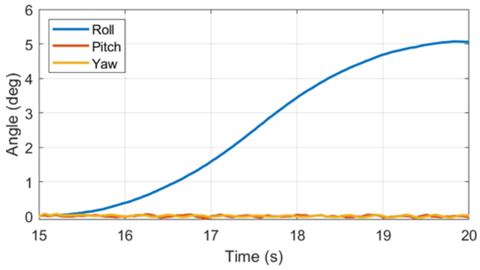

(b)

Figure 9: (a) Position and (b) attitude plots for the 5deg roll-axis drag

ing coefficient that produced the lowest RMS reaction force/moment is considered the optimal. Through observation of position and attitude plots, a large amount of oscillations was noted for low damping cases. This could be due to amplification of uncertainties and the dynamics which in turn cause deviations between the setpoint and the measured position and attitude, resulting in larger control efforts to stabilize the system. This is further shown by the control input, horizontal thrust, as shown in Figure 10. At low damping, $c_x = 0.05Ns/m$, severe oscillations depict marginally stable behavior. Hence, the high peaks at low damping coefficients suggests that a compromise is required between the level of oscillations that can be tolerated and a comfortable reaction force.

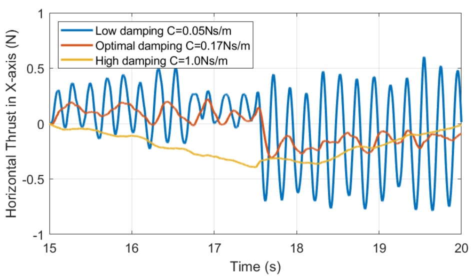

Figure 10: Control input of horizontal thrust for three levels of damping for a 1m x-axis drag. Calculated by taking the x-axis horizontal component of the total thrust

Figures 8(a) and (b) illustrate the position and attitude responses during the 1m x-axis drag at optimal parameters. The DoFs other than the interacted axis are shown to maintain constant values throughout the duration of interaction. Insignificant changes in the attitude demonstrates the capability of a fully-actuated UAV, where the decoupled translational and rotational axes enable safe, intuitive interactions.

Optimization of a roll-axis drag demonstrates the novelty of the work in this paper and the ability of a fully-actuated drone to hold a non-zero roll setpoint without translating, as shown in Figure 9. This is another advantage of a fully-actuated drone over its underactuated counterpart, where interaction can occur in two additional DoFs (ie. roll and pitch). This allows for a greater range of applications, such as the need for tilted station keeping during physical interaction.

Similar trends as seen in Section 4.3 are observed across the z and yaw axes. Table 1 summarizes the optimal parameters found through simulations for the four DoFs and the corresponding reaction forces (F_r) and moments (τ_r). The reaction forces can be compared to the weight of the UAV (12.4N). The optimal x-drag and average z-drag reaction forces are 0.7% and 3.5% of the UAV's weight, respectively.

5 FREE FLIGHT TESTS

5.1 Test System

Figure 11 illustrates the free flight test system used. It consists of four main components:

	Parameter range, $M = 0$	Optimal $c_i(Ns/m)$	F_r, τ_r
x-drag	$c_x = 0.05 - 0.5$	0.17	$0.085N$
z-drag (up)	$c_z = 1.2 - 2.0$	1.62	$0.49N$
z-drag (down)	$c_z = 1.2 - 2.0$	1.27	$0.38N$
Roll-drag	$c_\phi = 0.3 - 0.6$	0.43	$0.014Nm$
Yaw-drag	$c_\psi = 0.01 - 0.5$	0.014	$0.015Nm$

Table 1: Summary of simulation optimal parameters obtained.

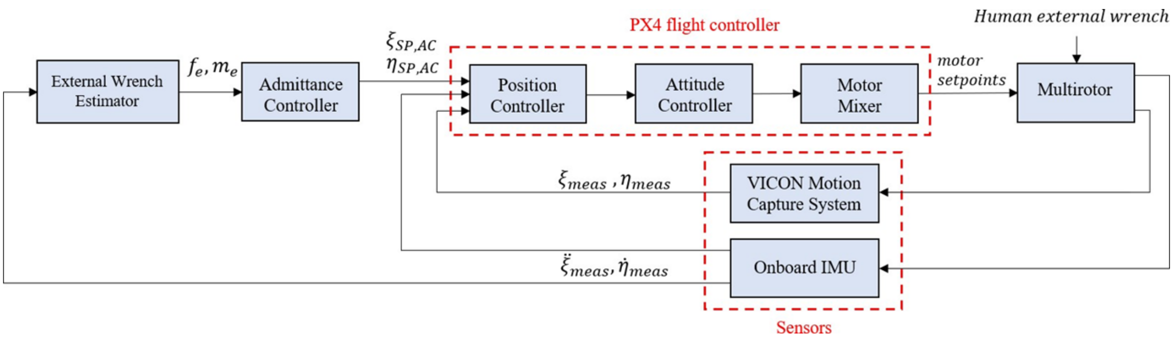

Figure 11: Experimental test system

1. The typical PX4 flight controller with cascaded P-PID controllers and the motor mixer.
2. The human external wrench directly applied by the human handler onto the UAV through physical contact.
3. Two types of sensing systems: the Vicon motion capture system with 12 cameras and an onboard IMU. The outputs of the two sensors are fused to compute the UAV's position and orientation information.
4. The sensor fusion, external wrench estimation and admittance controller setpoint computation are implemented and performed onboard the Pixhawk 4 mini control hardware.

Figure 12 depicts a handler performing PHDI in the motion capture lab.

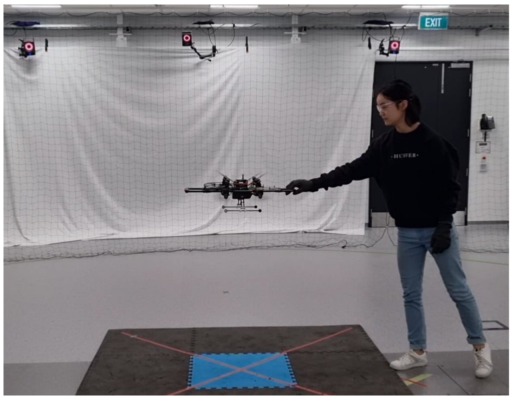

Figure 12: Free-flight test setup in motion capture lab with Vicon system

5.2 *Test Procedure*

To validate simulation results, the following drag interactions were experimented and optimized with the following cases:

1. x-translational drag - $\boldsymbol{\xi_f} = (0.5, 0, 0)m$
2. Yaw-drag - $\boldsymbol{\eta_f} = (0, 0, 45)deg$
3. Combined interaction - $\boldsymbol{\xi_f} = (0.75, 0, 1.5)m$

Note that testing for a roll-axis drag was not performed on the UAV used in this paper due to the tendency for the actuators to saturate with small moment applications. Additionally, due to the large spread of reaction forces at each damping coefficient in the z-axis testing, the optimization results have been omitted in this paper.

The dead band for each axis was first tuned to allow for any minor disturbances to be disregarded and to only update admittance controller setpoints once forces or moments were outside a specific range. The dead band also defines the duration of interaction. This was done by station keeping the UAV whilst logging the estimated forces and moments. Based on the residual estimated wrench, the dead band was determined for each axis.

Parameter m_i was gradually decreased from the default value. Zero m_i values were tested, however, this resulted in unstable and oscillatory behavior, thus, a non-zero value was selected for each of the axes. For each drag interaction experimented, different damping values were tested, and each combination of parameters was repeated 10 times to obtain averages. The lower bound was determined based on visual and log observations; significant oscillatory responses at low damping affected results and risked the safety of the handler, thus were omitted.

Table 2 shows the mean and maximum velocities encoun-

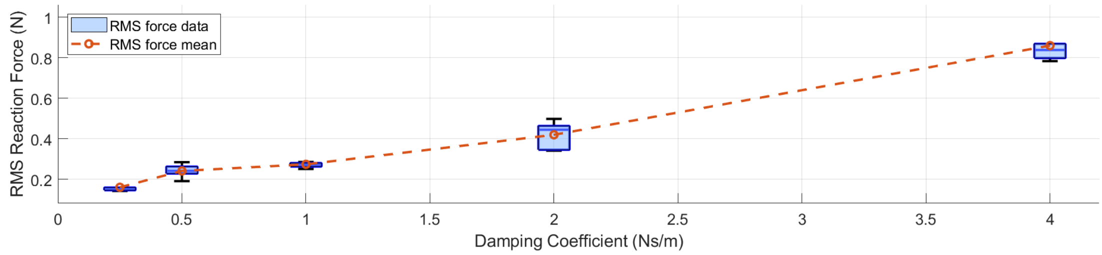

(a)

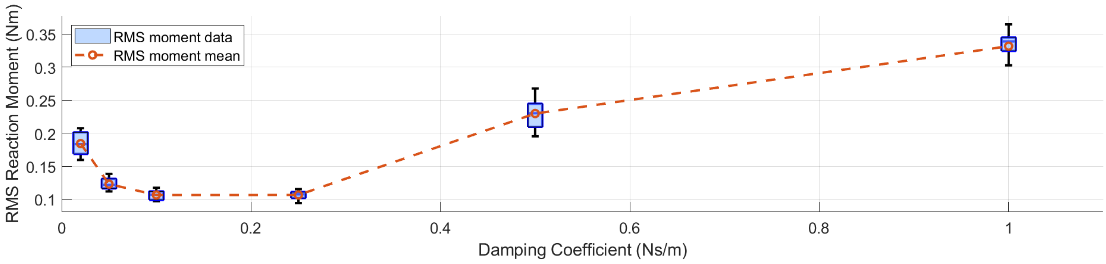

(b)

Figure 13: (a) Relationship between changing c_x with RMS reaction force for the x-axis drag in free flight tests at $m_x = 0.1$ and (b) relationship between changing c_ψ with RMS reaction moment for the yaw-axis drag in free flight tests at $m_\psi = 0.1$

tered during interaction in each axis. The maximum velocity recorded can therefore be quantified as the upper limit of the interaction rate for the sets of free flight tests performed in this study. Reaction forces and moments are directly related to the velocity during interaction, therefore consistent velocities are required to achieve repeatability.

	Mean velocity	Maximum velocity
x-drag	$0.21m/s$	$0.27m/s$
Yaw-drag	$0.29rad/s$	$0.39rad/s$

Table 2: Mean and maximum velocities during free flight tests for each tested axis

5.3 Results and Discussion

In Figures 13(a) and (b), the trends observed align well with those seen in simulation results. As the damping coefficient increases, the RMS reaction force and moment increase. The large spread observed in the data may be due to inconsistencies by the handler during interaction. In the x-axis drag tests, any c_x lower than 0.25Ns/m resulted in unsafe oscillatory behavior, thus results have been omitted. In the yaw-axis drag tests, an optimal point, $c_\phi = 0.1Ns/m$, is observed, as also depicted in the trends shown in simulations.

Table 3 summarizes the optimal parameters obtained through experimental testing. Compared to the weight of the UAV (12.4N), the optimal x-axis drag force is 1.3%.

Figure 14 shows the experimental data for a combined interaction where the UAV was physically interacted in multiple

	Parameter range	Optimal $c_i(Ns/m)$	F_r, τ_r
x-drag	$c_x = 0.25 - 4$	0.25	$0.16N$
Yaw-drag	$c_\psi = 0.02 - 1$	0.1	$0.11Nm$

Table 3: Summary of free flight optimal parameters obtained.

axes simultaneously, namely x-axis drag and z-axis drag. The shaded area on the graph depicts the region in which interaction occurred. The position appear to follow the setpoints well. At the end of the interaction, the position and attitude is held. A combined interaction shows that the axes are decoupled and a multi-axis interaction does not impact the UAV's ability to follow and hold setpoints.

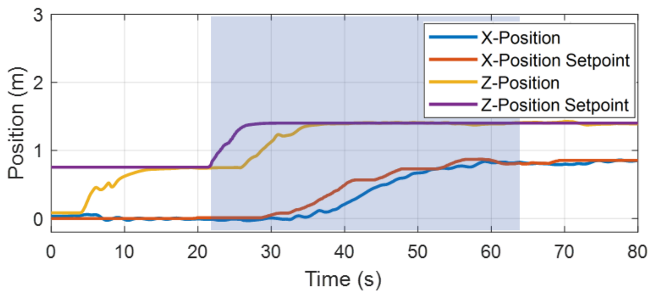

Figure 14: Combined interaction position graph using optimal parameters in free flight testing

6 CONCLUSIONS

This paper presents a novel analysis of admittance control on a compact, fully-actuated UAV for the purpose of human drone physical interaction. The main contribution is the optimization of the admittance controller in multiple translational and rotational axes to allow users to safely and intuitively interact with the UAV with minimal reaction forces and moments. The performance of the admittance controller was validated through simulations and experimental testing; optimal reaction forces of 0.7% and 1.3% of the UAV's weight were achieved for translation in the horizontal axis in simulations and free flight tests, respectively.

Future work will involve experimentally testing the roll and pitch-drag interactions to validate simulation results. Furthermore, an approach to differentiate between disturbance and human wrench will be investigated.

7 ACKNOWLEDGMENTS

The authors would like to acknowledge Pedro Mendes for his assistance and support for the work in this paper and the Drone Technology Research Group at the University of Auckland for their continuous feedback.

REFERENCES

[1] Silvia Mirri, Catia Prandi, and Paola Salomoni. Human-drone interaction: state of the art, open issues and challenges. In *Proceedings of the ACM SIGCOMM 2019 Workshop on Mobile AirGround Edge Computing, Systems, Networks, and Applications*, pages 43–48, 2019.

[2] Kei Nitta, Keita Higuchi, Yuichi Tadokoro, and Jun Rekimoto. Shepherd pass: ability tuning for augmented sports using ball-shaped quadcopter. In *Proceedings of the 12th International Conference on Advances in Computer Entertainment Technology*, pages 1–7, 2015.

[3] Felix Huppert, Gerold Hoelzl, and Matthias Kranz. Guidecopter-a precise drone-based haptic guidance interface for blind or visually impaired people. In *Proceedings of the 2021 CHI Conference on Human Factors in Computing Systems*, pages 1–14, 2021.

[4] Jonas Auda, Nils Verheyen, Sven Mayer, and Stefan Schneegass. Flyables: Haptic input devices for virtual realityusing quadcopters. In *Proceedings of the 27th ACM Symposium on Virtual Reality Software and Technology*, pages 1–11, 2021.

[5] Sujit Rajappa, Heinrich H Bülthoff, Marcin Odelga, and Paolo Stegagno. A control architecture for physical human-uav interaction with a fully actuated hexarotor. In *2017 IEEE/RSJ International Conference on Intelligent Robots and Systems (IROS)*, pages 4618–4625. IEEE, 2017.

[6] Sean Braley, Calvin Rubens, Timothy Merritt, and Roel Vertegaal. Griddrones: A self-levitating physical voxel lattice for interactive 3d surface deformations. In *UIST*, volume 18, page D200, 2018.

[7] Jessica R Cauchard, Jane L E, Kevin Y Zhai, and James A Landay. Drone & me: an exploration into natural human-drone interaction. In *Proceedings of the 2015 ACM international joint conference on pervasive and ubiquitous computing*, pages 361–365, 2015.

[8] Z Jeremy Chen, Jérémie XJ Bannwarth, Karl A Stol, and Peter J Richards. Analysis of a multirotor uav with tilted-rotors for the purposes of disturbance rejection. In *2018 International Conference on Unmanned Aircraft Systems (ICUAS)*, pages 864–873. IEEE, 2018.

[9] Markus Ryll, Giuseppe Muscio, Francesco Pierri, Elisabetta Cataldi, Gianluca Antonelli, Fabrizio Caccavale, and Antonio Franchi. 6d physical interaction with a fully actuated aerial robot. In *2017 IEEE International Conference on Robotics and Automation (ICRA)*, pages 5190–5195. IEEE, 2017.

[10] Stéphane Caron, Abderrahmane Kheddar, and Olivier Tempier. Stair climbing stabilization of the hrp-4 humanoid robot using whole-body admittance control. In *2019 International conference on robotics and automation (ICRA)*, pages 277–283. IEEE, 2019.

[11] Zhijun Li, Bo Huang, Zhifeng Ye, Mingdi Deng, and Chenguang Yang. Physical human–robot interaction of a robotic exoskeleton by admittance control. *IEEE Transactions on Industrial Electronics*, 65(12):9614–9624, 2018.

[12] Federico Augugliaro and Raffaello D'Andrea. Admittance control for physical human-quadrocopter interaction. In *2013 European Control Conference (ECC)*, pages 1805–1810. IEEE, 2013.

[13] Arvid QL Keemink, Herman van der Kooij, and Arno HA Stienen. Admittance control for physical human–robot interaction. *The International Journal of Robotics Research*, 37(11):1421–1444, 2018.

[14] Teodor Tomić, Christian Ott, and Sami Haddadin. External wrench estimation, collision detection, and reflex reaction for flying robots. *IEEE Transactions on Robotics*, 33(6):1467–1482, 2017.

[15] PH Souza and Karl Stol. Analysis and design of a novel fully-actuated compact multirotor. In *Australasian Conference on Robotics and Automation (ACRA)*, 2021.

[16] Christopher Banks, Antonio Bono, and Samuel Coogan. Physical human-uav interaction with commercial drones using admittance control. *IFAC-PapersOnLine*, 54(20):258–264, 2021.